

ResearchSpace@Auckland

Version

This is the Accepted Manuscript version. This version is defined in the NISO recommended practice RP-8-2008 <http://www.niso.org/publications/rp/>

Suggested Reference

Chen, G., Liss, K. -D., & Cao, P. (2014). In situ observation and neutron diffraction of NiTi powder sintering. *Acta Materialia*, 67, 32-44.
doi: 10.1016/j.actamat.2013.12.013

Copyright

Items in ResearchSpace are protected by copyright, with all rights reserved, unless otherwise indicated. Previously published items are made available in accordance with the copyright policy of the publisher.

© 2015, Elsevier. Licensed under the [Creative Commons Attribution-NonCommercial-NoDerivatives 4.0 International](http://creativecommons.org/licenses/by-nc-nd/4.0/)

<http://www.sherpa.ac.uk/romeo/issn/1359-6454/>

<https://researchspace.auckland.ac.nz/docs/uoa-docs/rights.htm>

An *In Situ* Observation and Neutron Diffraction of NiTi Powder Sintering

Gang Chen¹, Klaus-Dieter Liss^{2,3}, Peng Cao^{1*}

¹Department of Chemical and Materials Engineering, The University of Auckland, Private Bag 92019, Auckland 1142, New Zealand

²Quantum Beam Science Directorate, Japan Atomic Energy Agency, 2-4 Shirakata-Shirane Tokai-mura, Naka-gun, Ibaraki-ken 319-1195, Japan

³Australian Nuclear Science and Technology Organisation, New Illawarra Road, Lucas Heights, NSW 2234, Australia

Abstract

This study investigated NiTi powder sintering behaviour from elemental powder mixtures of Ni/Ti and Ni/TiH₂ using *in situ* neutron diffraction and an *in situ* scanning electron microscope. The sintered porous alloys have open porosities ranging from 2.7 % to 36.0 %. In comparison to the Ni/Ti compact, dehydrogenation occurring in the Ni/TiH₂ compact leads to less densification yet higher chemical homogenisation only after high temperature sintering. For the first time, a direct evidence of the eutectoid phase transformation of NiTi at 620 °C is reported by *in situ* neutron diffraction. A comparative study of cyclic stress-strain behaviours of the porous NiTi alloys made from Ni/Ti and Ni/TiH₂ compacts indicate that the samples sintered from the Ni/TiH₂ compact exhibited a much higher porosity, larger pore size, lower fracture strength, **lower close-to-overall porosity ratio and lower Young's modulus**. Instead of enhanced densification by the use of TiH₂ as reported in the literature, this study shows an adverse effect of TiH₂ on powder densification in NiTi.

Keywords: Shape memory alloys; Porous material; Reactive sintering; Mechanical behaviour; Hydrogen desorption

*Corresponding author, tel: +64-9-923 6924, fax: +64 -9-373 7463; email: p.cao@auckland.ac.nz (P. Cao)

1. Introduction

With the combination of unique shape memory effect (SME) and pseudoelastic (PE) properties with high strength, large energy absorption, good corrosion resistance and excellent biocompatibility, equiatomic NiTi has a wide range of applications such as

mechanical couplings, actuators and medical devices [1]. A few comprehensive reviews have been reported on the fabrication technologies of NiTi [2-4]. Porous NiTi alloys have been receiving increasing interest in biomedical applications because a porous structure not only further decreases their Young's modulus but also promotes bone tissue ingrowth. In the regime of manufacturing techniques for cellular NiTi alloys, a conventional press-and-sinter process is a widely used simple and cost-effective technique [4]. In terms of starting powder selection when the press-and-sinter method is introduced, blended elemental (BE) powders are generally preferred to pre-alloyed (PA) powders. This is because BE powders are not only much more affordable but with much better compressibility as compared with PA powders.

Recently, the enhanced densification of using TiH₂ as a replacement of Ti powder has been realised in titanium and its alloys powder metallurgy (PM) [5, 6]. The possible reasons for the enhanced densification observed in Ti alloys when TiH₂ is used were summarized by Wang et al. [7]. First, TiH₂ powder has better compressibility due to reduced cold welding between TiH₂ particles and significant powder fragmentation during compaction [8], thus achieving a high green density. Second, TiH₂ helps reduce the oxygen content in sintered Ti because dehydrogenation provides a reducing sintering atmosphere [9]. Third, TiH₂ has better sinterability: > 99 % sintered density is ready to achieve. This may be the result of the defects formed during the dehydrogenation process, which accelerates mass transport for densification [8]. Because of these attributes, many Ti alloys have been explored using TiH₂ powder, including pure titanium, Ti-6Al-4V, Ti-5Al-2.5Fe and TiAl [6, 8, 10-13]. In the case of PM NiTi, the use of TiH₂ also seems to result in a higher degree of sintering, reduced pore size and more uniform pore size distribution [14-18]. However, this enhanced densification is debatable and the sintering mechanism when TiH₂ is involved is not well understood. Recently, Robertson and Schaffer [19] observed a discouraging densification and a much larger porosity when TiH₂ powder is used. This is consistent with our recent study [20]. However, they believed the resultant higher porosity is not due to the hydrogen release, but the evaporation of contaminant in the TiH₂ powder. It has to be pointed out that the particle size of TiH₂ used in many reports such as Refs. [14-16] is much smaller than Ti. Therefore, the Ni/TiH₂ compact usually has a higher green density than the Ni/Ti compact, and thus it is not surprising to observe a higher sintered density in the Ni/TiH₂ compact. Considering these, it is not clear that the observed higher densification is caused by the dehydrogenation of TiH₂ or simply because of the higher green density as a result of smaller particle size in TiH₂ compact. As a matter of fact, in the production of porous NiTi alloys TiH₂ powder is

normally used as a foaming agent as it does in aluminum metallic foams. Thus, it is of great importance to clarify whether or not the use of TiH_2 benefits densification in PM NiTi alloys, and specifically whether or not the dehydrogenation enhances sintering.

Apart from the densification, another equally important aspect in powder metallurgical NiTi is how to achieve a single B2 phase. Even though the PM techniques have successfully produced NiTi alloys, these products are never of single phase. The as-sintered NiTi alloys always contain other phases, such as NiTi_2 , Ni_3Ti or Ni_4Ti_3 . Some reports attribute this to the incomplete reaction between Ni and Ti powders [21] or the eutectoid phase transformation occurring at 630 °C [22-25]. However, many others do not believe the existence of such eutectoid decomposition [26-32]. Clarification of this eutectoid transformation has been a long-sought challenge in the past six decades [32]. In 1950, Duwez and Taylor [22] first reported the decomposition of NiTi into Ni_3Ti and NiTi_2 at 800 and 650 °C. However, a subsequent study in 1953 by Margolin et al. [26] negated such a eutectoid reaction in a high purity NiTi. This problem was also investigated by Koskimaki et al. [24] who found NiTi eutectoidally decomposes into Ni_3Ti , NiTi_2 and an intermediate phase ('X-phase' in their paper) upon prolonged aging for one month at 600 °C. In contrast, Nishida et al.'s report [31] revealed no such secondary phases present in a 50Ni-50Ti alloy upon furnace cooling and water quenching from 1000 °C. In the same report [31], Nishida et al. also investigated the precipitation sequence of intermetallics during ageing of a Ni-rich 52Ni-48Ti alloy, which follows $\text{NiTi} \rightarrow \text{Ni}_4\text{Ti}_3 \rightarrow \text{Ni}_3\text{Ti}_2 \rightarrow \text{Ni}_3\text{Ti}$ with Ni_3Ti being the equilibrium phase. They claimed no eutectoid reaction in their system. The argument and debate of whether or not the eutectoid reaction exists have been recently reviewed by Otsuka and Ren [32]. They suggest that this eutectoid phase transformation seems unrealistic, since no direct evidence had been obtained thus far [37]. Nevertheless, we should note that all of these studies utilised *ex situ* laboratory X-ray diffraction (XRD), which suffers from insufficient penetration into metallic samples and lack of intensity. This technical incapability can be overcome with the development of high-energy X-rays at modern synchrotron and neutron diffraction, available at reactors and spallation sources [33, 34]. The synchrotron and neutron radiations are able to penetrate into bulk metals and have been successfully employed for *in situ* studies in metal sintering and phase transformations [35]. The beam intensities allow information from the bulk of material to be followed on short time scales, while undergoing an *in situ* heating to cooling cycle to observe phase transformation.

To the best of our knowledge, a comparative study using Ti and TiH₂ powders to fabricate NiTi alloys has not been available; more specifically the influence of hydrogen release from TiH₂ powder on densification and chemical homogenisation, and the first-hand evidence of eutectoid decomposition are lacking. This work is an companion of our recently published report [36]. In the present study, the *in situ* neutron diffraction technique was applied, for the first time, to the quantitative investigation of NiTi powder sintering and to the phase evolution upon *in situ* heating and cooling. The *ex situ* laboratory XRD was also performed in companion with the neutron diffraction. We also used an environmental scanning electron microscopic technique to observe *in situ* microstructural evolution during dehydrogenation of TiH₂. In brief, the purpose of this study is (1) to investigate the microstructure, phase transformation and mechanical properties of NiTi alloys prepared from powders of Ni with either elemental Ti or TiH₂; (2) to investigate the effect of hydrogen release during sintering on densification, chemical homogenisation and mechanical properties; (3) to present a direct proof to clarify whether or not the eutectoid reaction happens during furnace cooling, by conducting the *in situ* neutron diffraction; and (4) to discuss the sintering mechanism involved in TiH₂ powder.

2. Experimental

2.1. Materials

The mean particle size of starting Ti, TiH₂ and Ni powders is 32.2, 24.6 and 16.4 μm, respectively. Two batches of powder mixture, i.e., Ni/Ti and Ni/TiH₂, both having a nominal composition of 51 at.% Ni and 49 at.% Ti, were gently mixed in a ball mill for 10 h. No binder or lubricant was added during mixing.

2.2. Pressing and sintering

After mixing, the powder mixture was compacted in a single-action steel die under 250 MPa pressure. Stearic acid as a lubricant was lightly applied to the die wall before filling the die cavity with powder, which was then pressed into cylinders of 12 mm diameter with three heights (i.e., 4, 10 and 20 mm for microstructural characterisation, neutron diffraction measurement and compression test, respectively). Subsequently, the 4 and 20-mm-thick green compacts were sintered in a vacuum furnace at 3×10^{-3} Pa. The release of hydrogen as a function of temperature and time was recorded with a real-time vacuum monitor. The heating profile is shown in Fig. 1, where two stages can be distinguished. The heating rate was 5

K/min The first stage of heating is designed for dehydrogenation of TiH₂ powder as reported in Ref. [18], while the second stage is to perform sintering. The final sintering was conducted at 1000, 1100 and 1200 °C respectively for 2 h and followed by furnace cooling. The pressure variation in the furnace chamber is also shown in Fig. 1. The samples were taken at prescribed time intervals as shown in Fig. 1 to study the microstructural and phase evolution. Only the samples after 1100 °C sintering were subjected to a further post-sintering treatment (PSed) in vacuum at 1000 °C for 6 h. The purpose of this post-sintering treatment intended to enhance final phase homogenisation and thus improve pseudoelastic properties.

2.3. *In situ* neutron diffraction and data analysis

Neutron diffraction measurements were carried out on the high-intensity diffractometer WOMBAT at the Australian Nuclear Science and Technology Organisation (ANSTO) [37]. The WOMBAT instrument uses monochromatic neutrons and is equipped with a two-dimensional, position sensitive area detector. The <311> reflection of a germanium crystal monochromator was used under asymmetric cut of 9.45° and take-off angle 90°, to define the incident beam. It was calibrated by an Al₂O₃ standard to a wavelength $\lambda=2.419$ Å and corresponding wave number $k=2.597$ Å⁻¹. The diffracted neutrons were collected on the cylindrical detector, which subtends an angular range from 26° to 146° on the sample in the diffraction plane and ~20° in the vertical, out of plane direction, spanning a total powder-diffraction range from 1.2 Å⁻¹ to 5.0 Å⁻¹. The WOMBAT instrument is equipped with a high temperature vacuum furnace (5×10^{-4} Pa), and the diffraction data are *in situ* recorded. The 2D diffraction patterns were collected every 30 seconds as the sample temperature was ramped up and then down. With the high flux on the WOMBAT instrument, 30 seconds patterns provided sufficient statistics, once the data were integrated azimuthally along the diffraction rings into 1D bins depending on diffraction angle 2θ . Instrument independent reciprocal space coordinates $Q = 4\pi/\lambda*\sin(\theta)$ were calculated from the 2θ value of each bin and were used for quantitative analysis. Due to the strong incoherent neutron scattering from hydrogen, the 10-mm-thick Ni/Ti and Ni/TiH₂ compacts were firstly pre-heated at 580 °C (i.e., specimen #2 in Fig. 1) in vacuum furnace to dehydrogenate TiH₂ powder. The pre-heated Ni/Ti sample and dehydrogenated Ni/TiH₂ sample were then wrapped by molybdenum wire and heated in the WOMBAT instrument to 650 °C with a heating rate of 40 K/min, after which the sintering profile follows the same heating profile as shown in Fig. 1 to 1100 °C for 2 h. The neutron diffraction was also recorded during furnace cooling. A C-type thermocouple was placed close to the sample surface to read and control temperature.

The Rietveld analysis was used for the full powder-diffraction pattern fitting to obtain quantitative values of the phase fractions throughout the *in situ* experiments [38]. A free Rietveld program *MAUD* was chosen for further batch processing. Each one-dimensional diffraction pattern was subsequently fed into Rietveld analysis to determine the phase fractions as a function of time or temperature. The Rietveld analysis began by setting up *MAUD* with a well fitted analysis file, which was then used for recursive fitting of the following data files. The batch running was repeated several times with different starting values and constraints to start the iterating process until there was a consistently good fitting throughout the entire run.

2.4. Microstructural characterisation

Porosity and density were measured by the Archimedes method as specified in the ASTM B962-08 standard. Instead of using conventional densification parameter, when TiH_2 is involved, Robertson and Schaffer [19] suggest densification be calculated as per $\Phi = (\rho_s / \rho_{th} - \rho_g / \rho'_{th}) / (1 - \rho_g / \rho'_{th})$. Here, ρ_{th} is the theoretical sintered density, ρ'_{th} is theoretical green density, ρ_s is sintered density while ρ_g is green density. If porosity is unchanged by the sintering process and complete dehydrogenation occurs, $\Phi = 0$. If the sintered density is equal to the theoretical sintered density, $\Phi = 1$. Negative values result if porosity is created during dehydrogenation or if swelling occurs during sintering. Microstructures of green and sintered compacts were observed using an environmental scanning electron microscope (ESEM, FEI Quanta 200F) equipped with an energy dispersive X-ray spectrometer (EDX). Phase constituents were identified using XRD (Bruker D2 Phaser). Differential scanning calorimetry (DSC, Netzsch 404 F3) was used to determine the various reactions of compacts during sintering with a heating rate of 40 K/min under flowing argon gas. The phase transformation temperatures under thermal conditions (without external stress applied) were determined using DSC (TA Instruments Q 1000) under flowing nitrogen gas atmosphere. The austenite finish (A_f) temperature of the specimens sintered from Ni/Ti compact at 1100 °C and post-treated at 1000 °C was 30.6 and 25.1 °C, respectively. In the case of Ni/TiH₂ compact, the A_f temperature was 20.2 and 9.3 °C, respectively, for the as-sintered and post-treated samples.

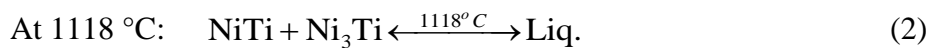
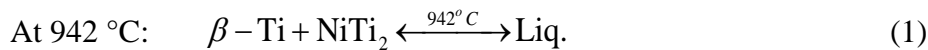
2.5. Compression test

Mechanical properties of the 20-mm thick samples after 1100 °C sintering were measured through compression testing on an MTS 810 universal machine with a loading rate of 0.6 kN/s at room temperature. An alignment cage was used to ensure parallelism of all samples during testing. Cylindrical compression samples (machined into 10.5 mm diameter and 15 mm height) were polished with 1200 and 4000 grit sand papers to smooth the ends, and finally the ends were greased before compression tests. Cyclic experiments were performed to investigate deformation and **pseudoelastic** recovery. The cylindrical samples were first compressed until a significant deflection in the linear elastic deformation portion of the stress-strain curve is observed or the stress level approaches to its fracture strength. After that they were unloaded to zero stress and the subsequent cycle follows immediately. Samples with various porosities and subjected to post sintering were performed to study the pseudoelasticity under 800 MPa compressive stress. **Three samples were used to ensure its repeatability in each cyclic experiment and an average mechanical property was reported.**

3. Results

3.1. Hydrogen release and thermal analysis

Fig. 2 compares the DSC traces of the 250-MPa-pressed Ni/Ti, Ni/TiH₂ and pure TiH₂ compacts with a heating rate of 40 K/min. It can be seen that there is a broad exothermic peak positioned at 821 °C for the Ni/Ti compact, beyond which an apparent endothermic peak develops with an onset temperature at 944 °C. This is immediately followed by an exothermic peak positioned at 968 °C. The fourth is an endothermic peak whose onset temperature is 1120 °C. The Ti-Ni binary phase diagram (Fig. 3) suggests two eutectic reactions:



The first broad exothermic peak for the Ni/Ti compact corresponds to the formation of intermetallic phases NiTi, NiTi₂ and Ni₃Ti via solid-state exothermic reactions between elemental Ti and Ni [39]. The second endothermic peak is a result of eutectic reaction (1) to form liquid Ti-rich phase. Once formed, this molten Ti-rich phase rapidly may spread throughout the powder compact and ignites an exothermic reaction with the Ni-rich phase to form intermetallics. The third small exothermic peak (at ~968 °C) is an indication of such

combustion reaction, although the extent of this combustion is small. At > 1118 °C, eutectic reaction (2) occurs and this is indicated by the fourth endothermic peak.

The evolution of hydrogen release from TiH_2 is an endothermic process [40], and it can be directly and precisely detected by an on-line pressure gauge monitor in the vacuum system. As illustrated in Fig. 1, the pressure varies with sintering time and temperature. Pressure starts to increase at about 220 °C and significantly rises up to 530 °C where it is stable for about 6×10^2 s followed by a dramatic drop until 580 °C. Finally, the pressure hardly changes after 800 °C. Referring to the DSC traces of the TiH_2 and Ni/TiH_2 compacts (Fig. 2), two endothermic events from ~ 400 to 750 °C pertain to hydrogen release. This finding is in accord with the results in Refs. [34, 41]. As compared with the Ni/Ti sample, the two dehydrogenation peaks may overlap the exothermic solid-state reaction events in the Ni/TiH_2 compact (Fig. 2). The endothermic peak at 942 °C is less apparent while the exothermic onset at ~ 980 °C indicates the combustion reaction. Again the last endothermic peak whose onset temperature is ~ 1138 °C is a result of the eutectic reaction (2). It is noteworthy that in the Ni/TiH_2 compact, the exotherm at 1013 °C and endotherm at 1148 °C are both postponed compared with the Ni/Ti compact.

3.2. XRD and phase evolution

Fig. 4 shows the XRD patterns of the Ni/Ti and Ni/TiH_2 compacts sintered at various temperatures and after post sintering. When the sintering temperature is < 800 °C, no intermetallic peaks could be observed except the Ti and Ni patterns for both compacts (Fig. 4). However, when the sintering temperature increases to 900 °C, most peaks of the Ti and Ni phases become very weak while intermetallic phases such as austenitic B2 NiTi and martensitic B19' NiTi , NiTi_2 and Ni_3Ti phases emerge in the case of the Ni/Ti compact (Fig. 4(a)). In contrast, a significant difference observed in the Ni/TiH_2 compact when compared with the Ni/Ti sample is that some unreacted Ni is still dominant after being sintered at 900 °C, Fig. 4(b). The co-existence of these phases in the as-sintered samples is further supported in the ESEM micrographs and EDX analysis (Fig. 5). For instance, at 900 °C the progressively grown intermetallic phases are indicated in Figs. 5(a) and 5(c) where apparent Ti-rich cores can be clearly seen. Upon closer examination of these cores, it is clear that these regions consist of two phases, as illustrated by the two different contrasts in Figs. 5(b) and 5(d). The composition of each of these two phases is difficult to determine by EDX analysis because of the fine scale of this two-phase microstructure. Nevertheless, the overall

composition for these cores determined by EDX analysis is Ti/Ni = 95.2/4.8 (at.%). Also the contrast in backscatter electron mode indicates that these two phases conform to the eutectoid structure forming via reaction of β -Ti \rightarrow α -Ti and NiTi₂ when β -Ti is cooled below 765 °C. This observation is in accord with Refs. [43, 44]. If the sintering temperature is further increased, the NiTi phase dominates, while the elemental phases thoroughly disappear for both compacts, Figs. 6(a) and 6(b). Meanwhile, it is interesting to note the pores in the sample sintered at 1100 °C become larger and much more isolated, as compared with the samples sintered at lower temperatures especially for the Ni/Ti compact (Fig. 6(a) cf. Fig. 5(a)). This is likely to be caused by transient liquid. Additionally, the Ni/TiH₂ compact after being sintered at 1100 °C exhibits much larger pore size and a greater porosity compared with the Ni/Ti compact (Fig. 6(b) cf. Fig. 6(a)). Some gaps between the newly born Ti and Ni particles are obvious, Fig. 5(c). A post-sintering treatment at 1000 °C for 6 h can improve the phase homogenisation as shown in Fig. 4, but the unwanted phases such as NiTi₂ and Ni₃Ti cannot be completely removed for the Ni/Ti compact. Such a post-sintering treatment for the Ni/TiH₂ compact completely removed Ni₃Ti, although NiTi₂ still persisted.

3.3. *In situ* neutron diffraction

Neutron diffraction patterns of the Ni/Ti and Ni/TiH₂ compacts collected as a function of time have been summarised in the 2D plot in Fig. 7. The grey scale values represent intensity as a function of scattering vector Q (i.e., $4\pi/\lambda \cdot \sin(\theta)$) on the abscissa and time on the ordinate. This diagram represents a series of conventional powder diffraction patterns, stacked on top of each other in time, while the sample temperature is varied as represented in the diagram to the right. The present work is focused on the phase transition during sintering to 1100 °C and then cooling down to ca. 187 °C.

As shown in Fig. 7(a), several intermetallic phases (i.e., B2 NiTi, Ni₃Ti, NiTi₂ and even Ni₄Ti₃) start to form when the temperature approaches 650 °C, at the expense of elemental Ni and Ti in the Ni/Ti compact. The presence of these intermetallic phases after being sintered at 800 °C for 1 h is fairly significant in the neutron diffraction pattern, while the XRD pattern does not reveal them, Fig. 4(a). The intensities of these intermetallic phases continue to increase until the temperature approaches about 970 °C at which the peaks of Ni, Ti, Ni₃Ti and Ni₄Ti₃ phases disappear, Fig. 7(a). An obvious difference between the Ni/TiH₂ and Ni/Ti sample (Fig. 7(a) cf. Fig. 7(b)) is observed, i.e., the temperature at which the amounts of Ni₃Ti, NiTi₂ and B2 NiTi start to increase significantly is almost 100 °C higher for the case

of the Ni/TiH₂ compact. In other words, the solid reactions between Ni and newly born Ti have been postponed. This is in accord with the DSC results (Fig. 2). Furthermore, there is no trace of Ni₄Ti₃ peaks appearing during the entire sintering and cooling cycle in the dehydrated Ni/TiH₂ compact, Fig. 7(b). However, once the temperature reaches over 880 °C, the intensity of each phase starts to change obviously. Only B2 NiTi and minor NiTi₂ remain for the pre-heated Ni/Ti compact, while the intensities of both NiTi₂ and Ni₃Ti peaks gradually reduce and almost disappear for the dehydrated Ni/TiH₂ compact during 1100 °C holding. The Mo peaks are noted because Mo wires were used to hold the samples in the instrument. A particular observation from the plots is the significant shift in position of the peaks when the temperature is relatively high. This is because of thermal expansion of crystal lattice. In addition, it is noteworthy that the peaks of previously disappeared secondary phases start to re-establish intensity for both compacts when the temperature is cooled to approximately 620 °C. This strongly indicates phase transformations, and most likely a eutectoid reaction, taking place at this temperature during furnace cooling.

3.4. Porosity and densification evolution

Fig. 8 displays the open porosity and densification of the Ni/Ti and Ni/TiH₂ compacts sintered at different temperatures. The open porosity increases slightly to 28.9±1.0 % when sintered at 580 °C for the Ni/Ti compact, Fig. 8(a). However, there is no reaction taking place at this temperature according to the DSC trace (Fig. 2) and XRD pattern (Fig. 4a). Thus, it is suggested that the increased porosity is attributed to the Kirkendall pore-forming mechanism because of the different inter-diffusion rates between Ni and Ti [32]. In contrast, the development of densification and open porosity of the Ni/TiH₂ compact is much more different from the Ni/Ti compact. Fig. 8(b) shows that the open porosity of the Ni/TiH₂ compact starts to increase greatly after 400 °C and reaches the maximum value of 36.0±0.2 % when sintered at 900 °C, while the densification does not change apparently. At a temperature between 400 and 800 °C, the DSC and XRD data reveal no reactions occurring to form intermetallic phases except the dehydrogenation of TiH₂ powder, Figs. 2 and 4(b). However, neutron diffraction in this temperature range does reveal the emergence of some intermetallic peaks, Fig. 7(b). The open porosity and densification difference from the Ni/TiH₂ compact is believed to stem from the effect of dehydrogenation of TiH₂. Since TiH₂ has a lower density (i.e., 3.90 g/cm³) than Ti (4.50 g/cm³), the porosity increases significantly due to shrinkage of the prior TiH₂ particle.

These hypotheses are further proved by the *in situ* ESEM images as shown in Fig. 9. Each compact was placed on a hot stage in the ESEM whose chamber was back filled with high purity argon gas (5N) to 300 Pa pressure. The sample was then heated up at a ramp rate of 5 K/min to 580 °C and held at this temperature for 1 h. *In situ* ESEM images were then continuously taken. As pictured in Fig. 9(b) there are some small pores (less than 1 μm) formed in the original Ni particles mainly along the Ni and Ti boundary after sintered at 580 °C for 1 h. By contrast, in the Ni/TiH₂ sample a number of important observations can be made. First, the volume of TiH₂ particles decreases, as shown by circles ‘a’ in Figs. 9(c) and 9(d). Second, new cracks emerge inside the prior TiH₂ particles, as a direct result of the volumetric change from TiH₂-to-Ti transformation (see arrow ‘A’ in Fig. 9(d)). Third, hydrogen release may push apart the originally closely-compacted particles, resulting in a gap in-between. These factors together lead to significant separation of prior particles, as indicated by arrows ‘B’ in Fig. 9(d), which visibly indicates the increased porosity after dehydrogenation. A similar result was reported by Robertson and Schaffer [45], but they did not provide micrographic evidence of the created porosity after dehydrogenation of TiH₂ powder.

Further increasing the temperature causes significant densification. The open porosity continuously decreases after 900 °C until it approaches 2.7±0.3 % while the densification rises to 0.68±0.01 at 1200 °C for the Ni/Ti compact, Fig. 8(a). For the Ni/TiH₂ compact, the open porosity decreases to 19.0±0.7 % (i.e., 16.3 % larger than that of the Ni/Ti compact) but the densification is only 0.19±0.01 at 1200 °C, Fig. 8(b). At a high temperature, e.g., 950 °C, the transient liquid phase sintering (LPS) starts to take place, which helps compact densification. Although the liquid phase could cause expansion of the compact (via liquid capillary effect) leaving pores behind in the prior titanium particle region [43, 44, 46], obviously densification effect outperforms expansion (Fig. 8). Additionally, it can be concluded that the hydrogen release from TiH₂ powder significantly increases the porosity of the Ni/TiH₂ sample, which thus has a great effect on the subsequent sintering.

3.5. Cyclic compressive properties

To study the effects of porosity and post sintering on the compressive properties, the samples were cyclically compressed to 800 MPa stress level and then completely unloaded. Fig. 10 compares the cyclic compressive properties of the sintered samples from the Ni/Ti and

Ni/TiH₂ compacts. Both samples were sintered at 1100 °C for 2 h. The Ni/Ti sintered sample could last all the five cycles, Fig. 10(a). However, the Ni/TiH₂ sintered sample failed at the third cycle with a residual strain of 2.19 %, Fig. 10(b). The stress-strain curves obtained from other samples, i.e., subjected to post-sintering treatment, are similar and the results are tabulated in Table 1. Some interesting aspects of pseudoelasticity (PE) can be found in these curves. Firstly, the secant modulus, which is computed by simply connecting the start and finish point on the unloading portion, almost remains unchanged with cycle number. This is different from the wrought NiTi alloys that usually show a monotonically decreased unloading secant modulus as the deformation is increased [1]. Secondly but more prominently, unloading does not follow the same path as loading/reloading so that a strain hysteresis develops. It is noted that the width of hysteresis **quickly diminishes** with cycle number. Thirdly, the pseudoelastic recovery strain (ϵ_{pe}) after each cycle decreases with cycle number, most strongly after the first cycle. The data of residual strain after the first and last cycles (ϵ_1 and ϵ_5), pseudoelastic recovery strain ϵ_{pe} after the first cycle and modulus are given in Table 1. The unloading secant modulus does not change, but the residual strain increases with cycle number. **Such observations have also been reported in Refs. [47, 48].** Meanwhile, the ϵ_{pe} value of the sample after post-sintering treatment (PSed) is greater than that of the sintered Ni/Ti but secant modulus hardly changes. In addition, the Young's modulus is always lower than the secant modulus in all cases. **In addition to the significantly larger porosity of the Ni/TiH₂ than that of Ni/Ti compacts, the Young's and secant moduli of the former compact are lower than those of the latter compact.**

Table 1 Cyclic compressive properties of the Ni/Ti and Ni/TiH₂ compacts sintered at 1100 °C and the sintered compacts after post-sintering (PSed) under 800 MPa compressive stress.

Sample	Overall porosity/%	ϵ_1 /%	ϵ_5 /%	ϵ_{pe} /%	Young's modulus/GPa	Secant modulus/GPa
Ni/Ti	15.0±0.9	1.01±0.01	1.43±0.03	1.65±0.06	11.5±0.7	13.8±0.5
Ni/Ti PSed	14.3±0.3	0.97±0.01	1.52±0.02	1.81±0.05	11.2±0.8	14.4±0.3
Ni/TiH ₂	30.9±1.1	2.01±0.05	/	1.00±0.05	9.3±1.2	13.4±0.2
Ni/TiH ₂ PSed	28±0.3	1.23±0.03	1.69±0.04	1.92±0.07	9.0±0.4	11.2±0.2

4. Discussion

4.1. Microstructural evolution involving in reactive sintering of elemental mixtures

Whitney et al. [43] investigated the mechanism of reactive sintering in a Ni/Ti powder compact using DSC and metallographic analysis. A conceptual model was proposed, as shown in Fig. 11, where the microstructure develops from a representative unit consisting of a Ti particle embedded in a Ni matrix. For simplicity, the final sintering temperature is set at 1100 °C in this model to exclude the eutectic reaction at 1118 °C. When this unit is heated to and/or held at a relatively low temperature (below the eutectic temperature of 942 °C), a few reactions occur including α -to- β transformation of Ti (endothermic), and the formation and growth of the NiTi₂, NiTi and Ni₃Ti intermetallic phases (exothermic), Fig. 11(b). Upon heating above 942 °C, the melting event associated with the eutectic reaction of β -Ti + NiTi₂ → L occurs and subsequent capillary flow of the melt will leave a pore behind the prior β -Ti particle, Fig. 11(c). Upon cooling to room temperature, the peritectic solidification results in the formation of NiTi₂ at the (β -Ti)/NiTi₂ interface [43], as described in Fig. 11(d) with dashed lines. Depending on the heating history, NiTi₂, Ni₃Ti or even Ni may exist along with the main phase NiTi, Fig. 11(d).

When TiH₂ is used, the microstructural and phase development follows the same conceptual procedures aforementioned, except that TiH₂ decomposes and causes particle fragmentation, which increases porosity and causes separation of prior particles in the compact, Fig. 11(f). Consequently, the pore size in the Ni/TiH₂ compact is larger compared with the Ni/Ti compact (Fig. 11(g) cf. Fig. 11(c)).

4.2. Effect of dehydrogenation on sintering

The decomposition of TiH₂ occurs between 300 and 800 °C [34, 41, 46, 49, 50]. This is confirmed by our real-time pressure monitoring and DSC results as shown in Figs. 1 and 2. During the transformation of TiH₂ to α -Ti, a volumetric reduction of 16.8 % occurs. In addition, the dehydrogenation enables activated surfaces of fresh Ti powders and creates high concentrations of lattice defects, thereby enhancing surface energy and atomic diffusion [49]. There have been a number of studies on sintering densification of titanium hydride powder in the literature [6, 8, 10-13, 19, 45], but no consensus has been reached. A comparison of the measured open porosity for the Ni/Ti and Ni/TiH₂ compacts after sintered at various temperatures is presented in Fig. 12. In this figure, the open porosity difference (i.e., $P_{Ni/TiH_2} -$

$P_{Ni/Ti}$) is plotted as a function of sintering temperature. Different from most reports in the literature, our study used similar particle size (Ti particle size: 32 μm vs. TiH_2 particle size: 25 μm) and therefore resulting in similar green open porosity (the relative green density is 73 % and 71 %, respectively for Ni/Ti and Ni/ TiH_2). The porosity in the Ni/Ti compact sparsely changes in this temperature range, Figs. 8(a) and 11(b). With sintering, however, the value of $P_{Ni/TiH_2} - P_{Ni/Ti}$ increases especially after 400 $^\circ\text{C}$ (e.g., 6.6 ± 0.7 %). This is a result of the hydrogen release in the Ni/ TiH_2 compact. As a consequence, the Ni/ TiH_2 compact attains the enlarged inter-particle spaces, particularly the space between Ni and new-born Ti, as evidenced by the *in situ* observation, Fig. 9(d). Additionally, internal pressure in the compact could be built up when hydrogen is released, unless the gas can be readily evacuated. The built-up gas pressure may also cause the loss of initially intimate contact between the pressed particles and increase the final porosity (decreasing **densification**). This finding is also confirmed in Ref. [51]. In contrast, the inter-particle space hardly changes in the Ni/Ti compact due to the pre-sintering metallurgical bonding. In other words, the diffusion distance between the particles becomes larger in the case of the Ni/ TiH_2 compact after the decomposition of TiH_2 , which also causes larger pores in Ni/ TiH_2 . It should be noted that the reaction kinetics not only depends on the temperature and time of powder sintering, but also on the diffusion distance. The increased diffusion distance in the Ni/ TiH_2 compact after dehydrogenation postpones the subsequent reactive sintering and discourages densification, although the new-born Ti particle surfaces are more active. This hypothesis is further supported by the Rietveld quantitative analysis (Fig. 13) from the neutron diffraction data. Shown in Fig. 13 is the weight fraction of various intermetallic phases in both compacts during sintering and furnace cooling. Comparing Fig. 13(a) with Fig. 13(b) reveals that the intermetallics formation was much delayed in the Ni/ TiH_2 compact, during the low temperature sintering. At the final high temperature **sintering** stage, the amount of B2 NiTi phase is greater in the Ni/ TiH_2 compact (99.3 wt.%) than that in the Ni/Ti compact (91.5 wt.%). Again this is a result of activated Ti surface and fast homogenisation associated with the new-born Ti particles after dehydrogenation. In summary, dehydrogenation affects densification in different ways depending on **the** sintering stage. In a low temperature sintering or initial sintering stage, hydrogen release increases the inter-particle diffusion distance and thereby retards densification and homogenisation. On the other hand, in the final sintering stage or at a high temperature, the new-born Ti particles are much more active and promote chemical homogenisation.

4.3. Phases clarification in the sintered compact

Fig. 13 reveals that upon cooling, the amount of NiTi phase decreases while other secondary phases such as Ni₃Ti and NiTi₂ increase their fractions. In other words, NiTi decomposes into Ni₃Ti and NiTi₂. As pointed out in Ref. [32], whether there exists a eutectoid of NiTi \rightarrow Ni₃Ti + NiTi₂ at 630 °C has been debated for 60 years. Our report is the first study using an *in situ* method to observe such decomposition of NiTi at 620 °C. It is interesting to note that the Ni₄Ti₃ phase, which is too tiny to be detected using laboratory XRD (Fig. 4(a)), is also eutectoidally precipitated in the Ni/Ti compact according to the high-intensity neutron diffraction. The XRD patterns (Fig. 4) show that the Ni/Ti compact sintered at 1100 °C contains a higher amount of Ni₃Ti and NiTi₂ phases than the Ni/TiH₂ compact. This is consistent with the quantitative analysis of neutron diffraction (Fig. 13). Based on the data reported in this study and discussion above together with the Ni-Ti phase diagram (Fig. 3), it is suggested that the presence of NiTi₂ and Ni₃Ti in the sintered parts by powder sintering could be equally attributed to the following six sources: (i) incomplete reaction between Ni and Ti particles, (ii) eutectic reaction: $L \rightarrow \text{NiTi} + \text{Ni}_3\text{Ti}$ at 1118 °C, (iii) peritectic reaction: $L + \text{NiTi} \rightarrow \text{NiTi}_2$ at 984 °C, (iv) eutectic solidification: $L \rightarrow \beta\text{-Ti} + \text{NiTi}_2$ at 942 °C, (v) eutectoid reaction: $\beta\text{-Ti} \rightarrow \alpha\text{-Ti} + \text{NiTi}_2$ at 765 °C and (vi) eutectoid decomposition of NiTi at 620 °C. These factors play in a subsequent manner during the sintering and cooling procedure, which leads to the current difficulty of obtaining single NiTi phase through powder sintering. Fig. 13 suggests that the NiTi₂ phase in the samples sintered at 1100 °C from both types of compact could be resulted from sources (i) and (vi). As shown in Fig. 13, the Ni₃Ti phase seems less stable than NiTi₂ and almost disappeared during holding at 1100 °C for both types of compact. Thus, the needle-like Ni₃Ti phase after 1100 °C sintering is likely due to the source (vi) – eutectoid reaction, and is schematically depicted in Figs. 11(d) and 11(h).

4.4. Modulus and pseudoelasticity

The stress-strain curves in Fig. 10 demonstrate a non-linear elastic deformation behaviour. Non-linear elasticity is typical for porous materials as a result of the elastic buckling of cell walls or edges during mechanical test [52]. Nevertheless, the existence of non-linear elasticity shown in Fig. 10 and ϵ_{pe} (Tables 1) is still prominent, indicating the reversible austenite-to-martensite phase transformation under stress [1]. The PE, moduli and strength are significantly influenced by pore structure and chemical homogenisation. Generally, higher porosity or larger pore size leads to lower fracture strength and the material collapses by

brittle crushing in compression [52]. This is confirmed in this study, Fig. 10. Compressive tests show that stress-induced martensitic transformation quickly diminishes after the first loading-unloading cycle. As the cycling proceeds, the accumulated residual strain increases and then levels off to a constant value. This behaviour seems to follow the general shape memory ‘training process’ [48]. In the subsequent cycles, the applied stress of 800 MPa may not be sufficient to initiate the austenite-to-martensite transformation on the remaining B2 austenitic phase and a further increased external stress is needed for the martensitic transformation [53]. In this study, the Ni/TiH₂ sintered sample shows better pseudoelasticity than that of the Ni/Ti sintered sample under the identical 800 MPa compressive stress (Fig. 10). This is because the Ni/TiH₂ sintered compact yielded more B2 austenitic phase than the Ni/Ti sintered compact. As shown in Fig. 13, after sintering the Ni/Ti compact yielded 78 wt.% of B2 NiTi phase while the Ni/TiH₂ compact yielded 89 wt.% B2 phase at room temperature.

The Young’s modulus of the Ni/Ti sintered compact was ~20% greater than that of the Ni/TiH₂ compact (Table 1). The following three factors should be taken into account. First, the calculated densification degree of the Ni/Ti and Ni/TiH₂ compacts after 1100 °C sintering is 0.44 ± 0.01 and -0.13 ± 0.01 , respectively. A higher densification would result in a higher elastic modulus. Second, in a porous material, a higher ratio of close-to-overall porosity would give rise to a higher elastic modulus [52]. This close-to-overall porosity ratio was $34.5 \pm 5.4\%$ and $1.5 \pm 1.4\%$ for the Ni/Ti and Ni/TiH₂ sintered compacts, respectively. Last, the phases present in the sintered compact affect the elastic modulus as well. It was found that the Ni/TiH₂ compact contained 5 wt.% NiTi₂ phase while the Ni/Ti compact contained 15 wt.% NiTi₂. The Young’s modulus of NiTi₂ is not available in the literature; nevertheless, a value of 90 GPa would be a reasonable approximation for NiTi₂ because its Young’s modulus should be in the range between pure Ti (~110 GPa [54]) and NiTi (~70 GPa [55]). A higher fraction of NiTi₂ in the Ni/Ti would lead to a higher modulus. All these three factors point to a higher elastic modulus for the Ni/Ti sintered compact.

It is noteworthy that the Young’s modulus of all compacts is in the range of 8~20 GPa, which is a good match with the human cortical bone [2]. However, the obtained porosity and pore size do not perfectly fulfill the pore prerequisites of implants, which require: interconnected and open porosity in the range of 30 to 80 % and pore size in the range of 100 to 600 μm [2]. This could be achieved by adjusting powder compaction and densification parameter or by introducing a temporary space holder with suitable particle size, however, at the expense of reduced fracture strength.

5. Summary

In this study, we fabricated porous NiTi alloys from Ni/Ti and Ni/TiH₂ powder compacts using a conventional press-and-sinter method. The effects of dehydrogenation and sintering parameters were investigated in terms of microstructure and mechanical properties using both *ex situ* and *in situ* techniques. The following conclusions can be drawn from this study.

- (1) The predominant phase identified in all the samples after sintered over 1000 °C is B2 NiTi phase with the presence of some minor phases. Both blended compacts after high temperature sintering demonstrate densification which increases with sintering temperature.
- (2) The proof is presented that the hydrogen release enlarges diffusion distance between particles in the Ni/TiH₂ compact and therefore causes sintering retardation, less densification and lower chemical homogenisation when sintered at a relatively low temperature, while achieving higher alloying when a high temperature is applied.
- (3) We presented the first piece of direct evidence showing eutectoid decomposition of NiTi at 620 °C during furnace cooling with an *in situ* neutron diffraction technique.
- (4) Dehydrogenation of TiH₂ powders causes a much higher porosity, larger pore size, **lower close-to-overall porosity ratio and smaller fraction of NiTi₂ phase** in the Ni/TiH₂ sintered compact as compared with the Ni/Ti compact. Such result causes lower fracture strength **and lower Young's modulus** for the Ni/TiH₂ sintered compact.

Acknowledgments

We acknowledge the financial support from Ministry of Business Innovation and Employment (MBIE), New Zealand. The China Scholarship Council (CSC) is acknowledged for providing a doctoral scholarship to Mr. Gang Chen. The authors are grateful to the technical assistance from Dr. Michael Hodgson and Mr. Saifang Huang at The University of Auckland, and Prof. Yuehui He at Central South University, China. The authors thank Prof. David C. Dunand at Northwestern University for helpful discussion. We also acknowledge the support of the Bragg Institute, Australian Nuclear Science and Technology Organisation (ANSTO), in providing the neutron research facilities used in this work. The authors would like to thank Australian Institute of Nuclear Science and Engineering (AINSE) Ltd for providing financial assistance (Award No. P2716) to enable work on WOMBAT to be conducted.

References

- [1] Yamauchi K, Ohkata I, Tsuchiya K, Miyazaki S. Shape memory and superelastic alloys: technologies and applications. Cambridge, U.K.: Woodhead Publishing, 2011.
- [2] Bansiddhi A, Sargeant TD, Stupp SI, Dunand DC. *Acta Biomaterialia* 2008;4:773.
- [3] Wen CE, Xiong JY, Li YC, Hodgson PD. *Physica Scripta* 2010;2010:014070.
- [4] Elahinia MH, Hashemi M, Tabesh M, Bhaduri SB. *Progress in materials science* 2012;57:911.
- [5] Ivasishin OM, Demidik AN, Savvakina DG. *Powder Metallurgy and Metal Ceramics* 1999;38:482.
- [6] Azevedo CRF, Rodrigues D, Beneduce Neto F. *Journal of Alloys and Compounds* 2003;353:217.
- [7] WANG H, FANG ZZ, SUN P. A CRITICAL REVIEW OF MECHANICAL PROPERTIES OF POWDER METALLURGY TITANIUM. Princeton, NJ, ETATS-UNIS: APMI International, 2010.
- [8] Wang HT, Lefler M, Fang ZZ, Lei T, Fang SM, Zhang JM, Zhao Q. *Key Engineering Materials* 2010;436:157.
- [9] Heidloff AJ, Rieken JR, Anderson IE, Byrd D, Sears J, Glynn M, Ward RM. *JOM* 2010;62:35.
- [10] Ivasishin OM, Savvakina DG, Froes FH, Mokson VC, Bondareva KA. *Powder Metallurgy and Metal Ceramics* 2002;41:382.
- [11] Bhosle V, Baburaj EG, Miranova M, Salama K. *Metallurgical and Materials Transactions A* 2003;34:2793.
- [12] Ivasishin OM, Eylon D, Bondarchuk VI, Savvakina DG. *Defect and Diffusion Forum* 2008;277:177.
- [13] Zhang JM, Yi JH, Gan GY, Yan JK, Du JH, Liu YC. *Advanced Materials Research* 2013;616-618:1823.
- [14] Li BY, Rong LJ, Li YY. *Journal of materials research* 1998;13:2847.
- [15] Li B-Y, Rong L-J, Li Y-Y. *Materials Science and Engineering: A* 2000;281:169.
- [16] Li B-Y, Rong L-J, Li Y-Y, Gjunter VE. *Metallurgical and Materials Transactions A* 2000;31:1867.
- [17] Chen G, Wen GA, Cao P, Edmonds N, Li YM. *Powder Injection Moulding International* 2012;6:83.
- [18] Chen G, Cao P, Wen G, Edmonds N, Li Y. *Intermetallics* 2013;37:92.
- [19] Robertson IM, Schaffer GB. *Powder Metallurgy* 2010;53:27.
- [20] Chen G, Cao P, Edmonds N. *Materials Science and Engineering: A* 2013;582:117.
- [21] Li BY, Rong LJ, Li YY, Gjunter VE. *Acta Materialia* 2000;48:3895.
- [22] Duwez P, Taylor JL. *Trans AIME* 1950;188:1173.
- [23] Poole DM, Hume-Rothery W. *J Inst Met* 1954-55;83:473.
- [24] Koskimaki D, Marcinkowski MJ, Sastri AS. *Trans AIME* 1969;245:1883.
- [25] Gupta SP, Mukherjee K, Johnson AA. *Mater. Sci. Eng.* 1973;11:243.
- [26] Margolin H, Ence E, Nielsen JP. *Trans AIME* 1953;197:243.
- [27] Purdy GR, Parr JG. *Trans AIME* 1961;221:636.
- [28] Hirano K, Ouchi K. *J. Japan Inst. Met.* 1968;32:613.
- [29] Wasilewski RJ, Butler SR, Hanlon JE, Worden D. *Metall. Trans.* 1971;2:229.
- [30] Bastin GF, Rieck GD. *Metall Trans* 1974;5:1917.
- [31] Nishida M, Wayman CM, Honma T. *MTA* 1986;17:1505.
- [32] Otsuka K, Ren X. *Progress in materials science* 2005;50:511.
- [33] Liss K-D, Bartels A, Schreyer A, Clemens H. *Textures and Microstructures* 2003;35:219.
- [34] Jiménez C, Garcia-Moreno F, Pfretzschner B, Klaus M, Wollgarten M, Zizak I, Schumacher G, Tovar M, Banhart J. *Acta Materialia* 2011;59:6318.
- [35] Schmoelzer T, Liss KD, Staron P, Mayer S, Clemens H. *Advanced Engineering Materials* 2011;13:685.
- [36] Chen G, Cao P. *Metallurgical and Materials Transactions A* 2013;44:5630.
- [37] Studer AJ, Hagen ME, Noakes TJ. *Physica B: Condensed Matter* 2006;385–386, Part 2:1013.

- [38] Rietveld H. *Journal of Applied Crystallography* 1969;2:65.
- [39] Hey JC, Jardine AP. *Materials Science and Engineering: A* 1994;188:291.
- [40] Viswanathan B, Murthy SS, Sastri MVC. *Metal hydrides: fundamentals and applications*: Springer, 1999.
- [41] Liu H, He P, Feng JC, Cao J. *International Journal of Hydrogen Energy* 2009;34:3018.
- [42] Massalski TB, Okamoto H, Subramanian PR, Kacprzak L. *Binary alloy phase diagrams*. Materials Park, OH: ASM International, 1990.
- [43] Whitney M, Corbin SF, Gorbet RB. *Acta Materialia* 2008;56:559.
- [44] Whitney M, Corbin SF, Gorbet RB. *Intermetallics* 2009;17:894.
- [45] Robertson IM, Schaffer GB. *Powder Metallurgy* 2010;53:12.
- [46] Igharo M, Wood IV. *Powder Metallurgy* 1985;28:131.
- [47] Saburi T. *TiNi shape memory alloys*. Cambridge: Cambridge University Press, 1998.
- [48] Nemat-Nasser S, Guo W-G. *Mechanics of Materials* 2006;38:463.
- [49] Bhosle V, Baburaj EG, Miranova M, Salama K. *Materials Science and Engineering: A* 2003;356:190.
- [50] Wu S, Liu X, Yeung KWK, Hu T, Xu Z, Chung JCY, Chu PK. *Acta Biomaterialia* 2011;7:1387.
- [51] Low RJ, Robertson IM, Schaffer GB. *Scripta Materialia* 2007;56:895.
- [52] Gibson LJ, Ashby MF. *Cellular Solids: Structure and Properties*: Cambridge University Press, 1999.
- [53] Miyazaki S, Imai T, Igo Y, Otsuka K. *MTA* 1986;17:115.
- [54] Leyens C, Peters M. *Titanium and titanium alloys: fundamentals and applications*: Wiley-VCH, 2003.
- [55] Greiner C, Oppenheimer SM, Dunand DC. *Acta Biomaterialia* 2005;1:705.

Figure Captions

Fig. 1-Heating profile of temperature vs. sintering time (left) and pressure variation (right) induced by hydrogen release from TiH₂ powder. Note pressure on the abscissa and temperature on the ordinate.

Fig. 2-DSC curves of Ni/Ti, Ni/TiH₂ and pure TiH₂ compacts with a heating rate of 40 K/min.

Fig. 3-Titanium-nickel binary phase diagram, **from 0 to 75 at% Ni. Redrawn from Ref. [42].**

Fig. 4-XRD patterns of the compact after sintering at different temperatures and after post-sintering treatment (PSed) from (a) Ni/Ti and (b) Ni/TiH₂.

Fig. 5-BSE images of samples sintered from the Ni/Ti compact at (a) 900 °C, (b) enlarged square area in (a); sintered from the Ni/TiH₂ compact at (c) 900 °C, (d) enlarged square area in (c).

Fig. 6-BSE images of samples after being sintered at 1100 °C from (a) Ni/Ti and (b) Ni/TiH₂.

Fig. 7-Neutron diffraction patterns as a function of time while temperature is ramped from the compact of (a) pre-heated Ni/Ti and (b) dehydrated Ni/TiH₂.

Fig. 8-The open porosity and **densification** development as a function of sintering temperature for the compact of (a) Ni/Ti and (b) Ni/TiH₂.

Fig. 9-BSE *in situ* images from the Ni/Ti compact (a) green and (b) 580 °C sintered for 1 h; the Ni/TiH₂ compact (c) green and (d) 580 °C sintered for 1 h. The arrows in (b) indicate the Kirkendall pores. The arrows in (c) and (d) indicate the increased gap or crack while the circle highlights the shrinkage of TiH₂ powder after dehydrogenation.

Fig. 10-Compressive load-unload-recovery cycles under the compressive stress of 800 MPa for the samples after 1100 °C sintered (a) Ni/Ti and (b) Ni/TiH₂. A total of 5 cycles was applied to each sample. Note that individual cycles have been shifted along the x-axis for clarity.

Fig. 11-Schematic model of microstructural evolution during reactive sintering and furnace cooling, (a)~(d) Ni/Ti and (e)~(h) Ni/TiH₂. Region < 942 °C is the solid-state reaction process below 942 °C. Dehydrogenation and separation of new-born Ti powders is shown in (f); Region > 942 °C is the LPS above 942 °C; Region cooling is final structure below 620 °C after furnace cooling. White lines and black dots embedded in the final NiTi domain indicate the needle-like Ni₃Ti and spherical NiTi₂ eutectoid precipitates formed during cooling.

Fig. 12-The evolution of open porosity difference between the Ni/TiH₂ and Ni/Ti compact as a function of sintering temperature.

Fig. 13-Weight fractions of the detected phases as a function of time (temperature) during *in situ* scan as achieved by Rietveld refinement analysis upon heating and cooling. (a) the Ni/Ti compact after being pre-sintered at 580 °C, (b) the Ni/TiH₂ compact after being pre-sintered at 580 °C and (c) heating and cooling profile as a function of time.